Zhou, X. *et al.* (2019). *Géotechnique* **69**, No. 7, 606–619 [https://doi.org/10.1680/jgeot.17.P.299]

Grain size and time effect on the deformation of rockfill dams: a case study on the Shuibuya CFRD

XIANG ZHOU*, GANG MA† and YIDA ZHANG*

The mechanical behaviour of coarse, granular geomaterials critically depends on their grain size distributions. In the settlement analysis of rockfill dams, however, the stress–strain curves obtained from specimens with reduced gradations are often used to approximate the behaviour of prototype rockfills. Accumulated evidence has shown that such practice can underestimate the settlement of concrete face rockfill dams (CFRDs), leading to unexpected damage of the concrete slabs and excessive leakage of the dam. In this paper, the recently developed rate-dependent breakage mechanics theory and breakage-energy scaling law is applied for the settlement analysis of the Shuibuya CFRD. The model is first calibrated using triaxial data from reduced specimens and then the parameters are extrapolated to represent prototype rockfills. The constitutive equations are implemented in a finite-element package and later applied to full-scale simulations of the dam, covering its construction, impoundment and operation phases. The predicted settlement profiles agree reasonably well with the data measured from the internal displacement gauges, thus corroborating the predictive capability of the new methodology. Finally, it is shown that neglecting the scaling and creep effect in the constitutive behaviour of rockfills will underestimate the maximum settlement of the dam by 14% and 18%, respectively.

KEYWORDS: compressibility; creep; dams; embankments; particle crushing/crushability; settlement

INTRODUCTION

Accurate prediction of the settlement of rockfill dams is hindered by several uncertainties: (*a*) rockfills used in dam construction are often provided by local, gravelly deposits, rock quarries or excavations that can have a variety of geological origins (e.g. schist, greywacke, slate) and grain sizes (e.g. maximum grain size D_{max} varying between 200 and 1000 mm) (Naylor *et al.*, 1986; Alonso *et al.*, 2011); (*b*) the internal stress of high dams can be as high as several megapascals, lasting for its entire service life (Wen *et al.*, 2017), during which the time-dependent deformation of rockfills becomes relevant. Characterising the mechanical behaviour of such a variety of rockfills at extended time scales is difficult given the spatial and temporal limitations of the laboratory testing programmes. The largest specimen that can be accommodated by large-scale triaxial devices is 1·13 m dia. and 2·5 m high, which corresponds to a D_{max} of 180 mm (Marsal, 1967, 1973). The common diameters for rockfill specimens are limited to under 1 m and thus require even smaller D_{max} (Marachi *et al.*, 1972; Chávez *et al.*, 2009; Ovalle *et al.*, 2014). This implies that specimens with reduced grain sizes have to be used to infer the properties of the prototype materials. Creep tests typically last for several months (Cheng & Ding, 2004), which prohibits a systematic characterisation of their time-dependent responses prior to dam construction. For these reasons, the grain size effect is routinely neglected in the settlement prediction of concrete face rockfill dams (CFRDs), assuming that the parameters calibrated from reduced specimens are representative of the original rockfills. Creep is sometimes considered in the finite-element (FE) analyses using empirical models with seven to nine parameters (Zhou *et al.*, 2010; Pramthawee *et al.*, 2017) that can only be determined through back-analysis. These simplifications and uncertainties have generally led to an underestimated settlement of large CFRDs. For example, at the design stage of the Shuibuya CFRD, the predicted maximum settlement 1·36∼1·92 m is significantly lower than the observed 2·5 m after 3 years of operation. Such under-prediction cannot be fixed by considering creep, which gives a maximum settlement of 2·05∼2·38 m. Other examples are listed in Table 1 (Zhu *et al.*, 2009). These underestimations have led to unconservative design of concrete slabs, thus increasing the risk of face cracking, dam leakage and damage of the affiliated infrastructures (e.g. crest highways).

This paper presents a strategy to incorporate the grain size and time effects in modelling rockfill dams and examine its predictive capability through a comprehensive case study. Specifically, the present authors integrate the rate-dependent breakage mechanics model recently developed by Zhang & Buscarnera (2017) with the breakage-energy scaling law proposed by Zhang *et al.* (2016) to formulate a new strategy for continuum-based settlement assessment of rockfill structures (see later section entitled 'Theory'). This model is uniquely equipped to study the scale and time effect in rockfill structures for the following reasons: (*a*) all of the model parameters have clear physical meanings and well-defined calibration procedures, which permits forward predictions of settlement based on laboratory tests prior to dam construction; (*b*) the scaling relation for this model has been thoroughly studied using existing data sets (Zhang & Buscarnera, 2014), fracture-mechanics analysis at grain scale (Zhang *et al.*, 2016), discrete-element method (DEM) modelling (Cil & Buscarnera, 2016) and micro–macro experiments (Sohn *et al.*, 2017), which permits a rational

Manuscript received 30 November 2017; revised manuscript accepted 23 July 2018. Published online ahead of print 28 August 2018.
Discussion on this paper closes on 1 December 2019, for further details see p. ii.
* Department of Civil, Environmental and Architectural Engineering, University of Colorado Boulder, Boulder, CO, USA.
† State Key Laboratory of Water Resources and Hydropower Engineering Science, Wuhan University, Hubei Province, P. R. China.

Downloaded by [UNIV OF ILLINOIS] on [05/02/20]. Copyright © ICE Publishing, all rights reserved.

Table 1. Examples of CFRDs that have experienced excessive settlement

Name	Height: m	Complete	Maximum vertical settlement: m	
			Predicted	Measured (year)
Tianshengqiao-I	178	1998	1·24∼2·05	3·47 (2000)
Hongjiadu	179·5	2005	0·76	1·42 (2005)
Sanbanxi	185·5	2006	0·8	1·56 (2007)
Shuibuya	233	2006	1·36∼1·92	2·5 (2009)

incorporation of the scaling effect in rockfill engineering. The performance of this framework is evaluated through a case study on the Shuibuya dam (Hubei, China), currently the tallest CFRD in the world (see later section entitled 'The Shuibuya CFRD'). This dam is heavily instrumented with settlement monitoring systems and the rockfills have been well characterised by large-scale triaxial tests, providing sufficient data for the calibration and benchmarking of the proposed framework. The constitutive model is implemented in a FE code and a FE mesh is constructed for the Shuibuya dam (see later section entitled 'UMAT implementation and FE model'). Predictive exercises and parametric studies are conducted to elucidate the impact of scaling and time on the deformation of CFRDs (see later sections 'Prediction results' and 'Discussion').

THEORY

Rate-dependent breakage mechanics

The rate-dependent breakage mechanics is an extension of the original theory by Einav (2007a, 2007b) to model the instantaneous and delayed crushing of granular materials and the accompanying inelastic strains. Following the hyperplasticity formalism (Houlsby & Puzrin, 2006), the model can be summarised by two scalar functions

$$\Psi\left(\varepsilon_{ij}^{\mathrm{e}}, B\right) = \frac{1}{2}(1-\vartheta B)\left(K\varepsilon_{\mathrm{v}}^{\mathrm{e}2} + 3G\varepsilon_{\mathrm{s}}^{\mathrm{e}2}\right) \tag{1}$$

$$w\left(\bar{E}_{\mathrm{B}}, \bar{\sigma}_{ij}, B\right) = \frac{E_{\mathrm{c}}\dot{B}_0}{2(1-B)^2}\frac{\bar{\varsigma}_{\mathrm{pB}}^{n/2+1}}{n/2+1} \tag{2}$$

where Ψ is the Helmholtz free energy and w is the flow potential; $\bar{\varsigma}_{\mathrm{pB}}\left(\bar{E}_{\mathrm{B}},\ \bar{\sigma}_{ij}\right) = \langle \bar{y}_{\mathrm{pB}}(\bar{E}_{\mathrm{B}},\ \bar{\sigma}_{ij})\rangle$ is the breakage overstress function that measures the distance from the current stress state to the yield surface $\bar{y}_{\mathrm{pB}}$ in dissipative stress space; $\langle\cdot\rangle$ is the Macaulay bracket; $\bar{E}_{\mathrm{B}}$ and $\bar{\sigma}_{ij}$ are dissipative stresses; superscript 'e' denotes the elastic component; $\varepsilon_{\mathrm{v}} = \varepsilon_{ii}$ and $\varepsilon_{\mathrm{s}} = \sqrt{(2/3)e_{ij}e_{ij}}$ are the volumetric and deviatoric strains respectively; ε_{ij} and $e_{ij} = \varepsilon_{ij} - (1/3)\varepsilon_{\mathrm{v}}\delta_{ij}$ are the strain tensor and its deviator, respectively; B is the Einav's breakage index serving as an internal state variable in the model (i.e. $B = 0$ for uncrushed state and $B = 1$ for completely crushed state); ϑ is the grading index; K and G are the bulk and shear modulus; E_{c} is the critical breakage energy, the physical meaning of which will be discussed in the next section; $\dot{B}_0$ is a fluidity parameter (inverse of viscosity); n is the corrosion index that characterises microscopically the stress-dependency of crack velocity in rock minerals (Atkinson, 1982; Oldecop & Alonso, 2007). Applying hyperelastic relations, equation (1) leads to an isotropic linear elastic model

$$\begin{aligned}\sigma_{ij} &= \frac{\partial\Psi}{\partial\varepsilon_{ij}^{\mathrm{e}}} = \frac{\partial\Psi}{\partial\varepsilon_{\mathrm{v}}^{\mathrm{e}}}\frac{\partial\varepsilon_{\mathrm{v}}^{\mathrm{e}}}{\partial\varepsilon_{ij}^{\mathrm{e}}} + \frac{\partial\Psi}{\partial\varepsilon_{\mathrm{s}}^{\mathrm{e}}}\frac{\partial\varepsilon_{\mathrm{s}}^{\mathrm{e}}}{\partial\varepsilon_{ij}^{\mathrm{e}}} \\ &= (1-\vartheta B)\left(K\varepsilon_{\mathrm{v}}^{\mathrm{e}}\delta_{ij} + 2Ge_{ij}^{\mathrm{e}}\right)\end{aligned} \tag{3}$$

$$E_{\mathrm{B}} = -\frac{\partial\Psi}{\partial B} = \frac{1}{2}\vartheta\left(K\varepsilon_{\mathrm{v}}^{\mathrm{e}2} + 3G\varepsilon_{\mathrm{s}}^{\mathrm{e}2}\right) \tag{4}$$

where E_{B} is the breakage energy quantifying the release of the stored energy upon the evolution of the grain size distribution (GSD) of the granular system. The flow potential equation (2) defines the inelastic response of the system and represents a major deviation from the original breakage mechanics theory. First, it is a non-homogeneous function which permits a rate-dependent growth of the internal variables (i.e. B, $\varepsilon_{\mathrm{v}}^{\mathrm{p}}$, $\varepsilon_{\mathrm{s}}^{\mathrm{p}}$) as opposed to the first-order homogeneous dissipation functions used in rate-independent hyperplastic models (Collins & Houlsby, 1997; Houlsby, 2014). Second, the breakage evolution law is motivated from the kinetics of fracture growth at grain scale rather than assumed a priori from curve-fitting exercises. The hypothesis is that the creep of a granular matrix subjected to high confining stresses is a smeared outcome of consecutive grain breakage events due to time-dependent fracture growth within particles (Fig. 1, more details can be found in Zhang & Buscarnera (2017)). A yield function $\bar{y}_{\mathrm{pB}}$ needs to be specified to complete the expression of w. This function is chosen to be identical with the original breakage model (Einav, 2007b)

$$\begin{aligned}\bar{y}_{\mathrm{pB}} = &\left\{\frac{\bar{E}_{\mathrm{B}}}{\sqrt{E_{\mathrm{B}}E_{\mathrm{c}}}/[(1-B)\cos\omega]}\right\}^2 \\ &+ \left\{\frac{\bar{p}}{\sqrt{E_{\mathrm{c}}/E_{\mathrm{B}}}\,p/[(1-B)\sin\omega]}\right\}^2 + \left(\frac{\bar{q}}{Mp}\right)^2 - 1 = 0\end{aligned} \tag{5}$$

where ω is the coupling angle that controls the energy dissipation allocated to grain breakage and frictional sliding; M is the critical stress ratio; $\bar{p} = \bar{\sigma}_{ii}/3$ and $\bar{q} = \sqrt{(3/2)\left(\bar{\sigma}_{ij} - \bar{p}\delta_{ij}\right)\left(\bar{\sigma}_{ij} - \bar{p}\delta_{ij}\right)}$ are the mean and deviatoric stresses in dissipative space, respectively. Enforcing Ziegler's orthogonality condition in the form of $\bar{E}_{\mathrm{B}} = E_{\mathrm{B}}$ and $\bar{\sigma}_{ij} = \sigma_{ij}$, equation (5) becomes a teardrop-shaped yield surface in true stress space that can simultaneously account for shear- and compression-induced yielding of granular soils. Such shape well represents the yielding data of typical rockfill materials (Alonso *et al.*, 2016). Finally, the inelastic evolution laws are derived according to the definition of flow potential (Houlsby, 2014)

$$\dot{B} = \frac{\partial w}{\partial\bar{E}_{\mathrm{B}}} = \dot{B}_0\cos^2\omega\varsigma_{\mathrm{pB}}^{n/2} \tag{6}$$

$$\begin{aligned}\dot{\varepsilon}_{ij}^{\mathrm{p}} = &\frac{\partial w}{\partial\bar{p}}\frac{\partial\bar{p}}{\partial\bar{\sigma}_{ij}} + \frac{\partial w}{\partial\bar{q}}\frac{\partial\bar{q}}{\partial\bar{\sigma}_{ij}} = \frac{E_{\mathrm{B}}\dot{B}_0}{p}\sin^2\omega\varsigma_{\mathrm{pB}}^{n/2}\left(\frac{\delta_{ij}}{3}\right) \\ &+ \frac{E_{\mathrm{c}}\dot{B}_0}{(1-B)^2}\frac{q}{M^2p^2}\varsigma_{\mathrm{pB}}^{n/2}\left(\frac{3}{2}\frac{s_{ij}}{q}\right)\end{aligned} \tag{7}$$

Downloaded by [UNIV OF ILLINOIS] on [05/02/20]. Copyright © ICE Publishing, all rights reserved.

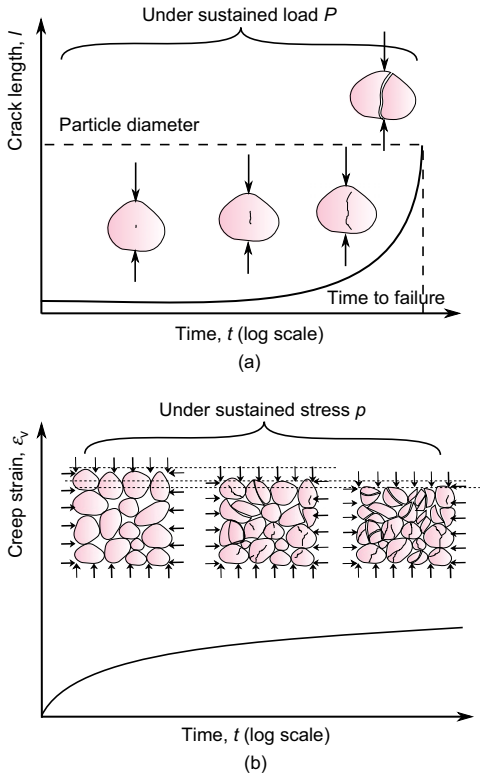

Fig. 1. Schematic representation of: (a) crack growth in a particle; (b) creep in a granular assembly (Zhang & Buscarnera, 2017)

where

$$\varsigma_{\mathrm{pB}}\left(E_{\mathrm{B}},\sigma_{ij}\right)=\left\langle y_{\mathrm{pB}}\left(E_{\mathrm{B}},\sigma_{ij}\right)\right\rangle =\left\langle \frac{(1-B)^2E_{\mathrm{B}}}{E_{\mathrm{c}}}+\left(\frac{q}{Mp}\right)^2-1\right\rangle \tag{8}$$

and $s_{ij}=\sigma_{ij}-p\delta_{ij}$ is the stress deviator; superscript 'p' denotes the plastic component. In summary, the model contains eight parameters that characterise the elastic, plastic, breakage and rate-dependent behaviour of rockfills. All of them can be calibrated from standard laboratory programs: the elastic moduli K and G can be determined from the elastic portion of the stress–strain curves; the critical stress ratio M (or equivalently the critical-state friction angle) can be measured by shearing the specimen to failure; the grading index ϑ reflects the relative distance between the initial GSD and the ultimate fractal GSD of the material; the coupling angle ω can be determined by matching the hardening portion of the stress–strain curves; the critical breakage energy E_{c} governs the size of the yield envelope and can be determined from the yielding stresses; the fluidity parameter $\dot{B}_0$ can be calibrated from creep tests; the corrosion index n can be inferred from the mineralogy of the rock or determined from the slope of the creep curves. A more detailed calibration procedure is discussed later in the section entitled 'UMAT implementation and FE model' with reference to the Shuibuya rockfills data.

Physically, $\dot{B}_0$ plays a similar role to fluidity in rheology as higher values of $\dot{B}_0$ promote larger inelastic flow (equations (6) and (7)). n alters the non-linearity of such rate-dependence, which is a parameter inspired from sub-critical fracture propagation analysis at grain scale (Zhang & Buscarnera, 2017). Figs 2(a) and 2(b) present the development of creep strain at a vertical stress of 10 MPa with various preloading rates. It can be observed that $\dot{B}_0$ controls the magnitude of the creep strain, while n controls the rate at which such creep strain develops and thus the shape of the creep curves. Figs 2(c) and 2(d) show the effect of critical breakage energy E_{c} on the compression and creep behaviours. It can be seen that E_{c} not only controls the size of the yield surface but also affects the amplitude of creep strain at prescribed stress levels. This is because a smaller yield surface creates a higher overstress for a given stress state and thus drives more viscoplastic straining. This feature allows the long-term behaviours of rockfill dependent on its short-term properties, which is consistent with the findings in Oldecop & Alonso (2007).

Scaling law

Rockfills consisting of larger grains exhibit smaller yield envelopes (Marsal, 1967; Marachi *et al.*, 1972), lower apparent elastic modulus (Ramon *et al.*, 2008; Zhou *et al.*, 2016) and higher percentage of particle breakage when loaded to the same stress state (Varadarajan *et al.*, 2003). These features are rooted in the size-dependent fracture strength of rock aggregates (Ovalle *et al.*, 2014; Tapias *et al.*, 2015). Zhang *et al.* (2016) have developed and validated the following relation to connect the particle fracture energy, E_{pc} (i.e. an index reflecting the geometry and fracture toughness of the particle), with the critical breakage energy, E_{c} (i.e. a parameter controlling the crushing resistance of the granular continuum)

$$E_{\mathrm{c}}=(1-\phi)\xi E_{\mathrm{pc}} \tag{9}$$

where ξ is an upscaling coefficient and ϕ is the initial porosity of the specimen. Such a proposition is again motivated from the micro–macro analogy between the energy storage in particles at the onset of crushing, and the energy input to trigger distributed grain crushing in the assembly. The parameter ξ encapsulates all the factors that affect such an upscaling process, including the distribution of force chains, the packing and gradation of the specimen, and the angularity of soil particles. The value of ξ ranges between 0·1 and 0·4, with an average value of 0·25 (Cil & Buscarnera, 2016; Sohn *et al.*, 2017). Using equation (9), grain-scale features such as particle diameter, angularity, the elastic and fracture properties can now enter the macroscopic description of granular assemblies. The analytical expressions of E_{pc} have been derived using linear elastic fracture mechanics (LEFM) and Weibull theory by assuming a variety of failure patterns (i.e. contact damage, central splitting and randomly distributed cracks) and contact models (i.e. Hertzian, conical and flat contact). In general, particle fracture energy scales with grain size d_{p} through a power law relation

$$E_{\mathrm{pc}}\propto d_{\mathrm{p}}^{-\lambda} \tag{10}$$

where λ is the scaling coefficient that depends on the failure and contact modes (Table 2). Combining equations (9) and (10), a useful scaling relation for E_{c} can be obtained

$$E_{\mathrm{c,field}}=E_{\mathrm{c,lab}}\left(\frac{D_{50,\mathrm{field}}}{D_{50,\mathrm{lab}}}\right)^{-\lambda} \tag{11}$$

where $E_{\mathrm{c,lab}}$ and $D_{50,\mathrm{lab}}$ are the critical breakage energy and the median grain size for the reduced specimen, respectively; $E_{\mathrm{c,field}}$ and $D_{50,\mathrm{field}}$ are those for the prototype rockfills. To apply equation (11), λ can be determined by plotting $E_{\mathrm{c,lab}}$ against $D_{50,\mathrm{lab}}$ from oedometer compression tests on specimens with different D_{50}. If such a test is not available, λ can be estimated from the existing data set or analytical solutions. Zhang & Buscarnera (2014) have calibrated E_{c} for a wide range of coarse-grained soils and found an average value of $\lambda=0{\cdot}826$, which is consistent with LEFM solutions for sub-rounded particles ($\lambda=0{\cdot}833$) (Zhang *et al.*, 2016).

Downloaded by [UNIV OF ILLINOIS] on [05/02/20]. Copyright © ICE Publishing, all rights reserved.

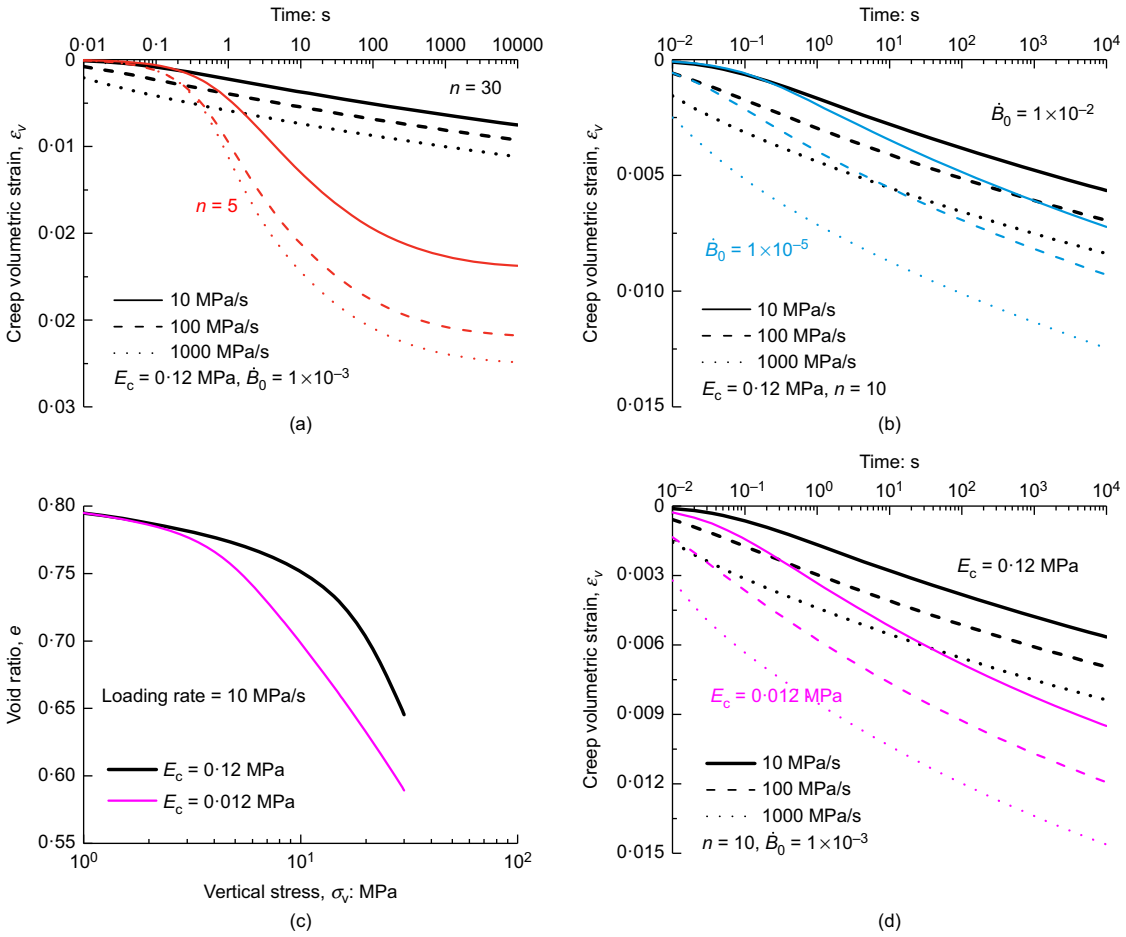

Fig. 2. Effects of n, $\dot{B}_0$ and E_c on the simulated creep and compression responses using Virginia Beach sand parameters under oedometer compression condition. All the creep curves are obtained under $\sigma_v = 10$ MPa. The preloading rates at which such stress is achieved are given in the keys

Table 2. Grain size dependency on the fracture energy of single particles due to different contact and failure models

$E_{pc} \propto d_p^{-\lambda}$	Central splitting	Contact damage	Randomly distributed cracking
Linear elasticity	1	N/A	6/w*
Hertzian elasticity	0·833	2·5	5/w
Conical elasticity	0·75	N/A	4·5/w

*w is the Weibull modulus, a constant that reflects the variability of the particle strength.

Breakage mechanics-based settlement analysis of rockfill dams

The workflow outlined in Fig. 3 is proposed to integrate the above theoretical components into a unified framework for predicting the settlement of rockfill dams. The step-by-step guidance for applying this procedure will be discussed later, together with the Shuibuya CFRD case study. It is worth mentioning that the current scaling procedure only applies to the parameter controlling the onset of grain breakage (i.e. the size of the yield surface) by way of E_c, with the assumption that the elastic and visco-plastic parameters are independent of grain size. The scaling effect on the elastic properties of granular soils is unclear at this stage (Wood & Maeda, 2008). On the one hand, the study by Salgado *et al.* (2000) showed that the stiffness of clean sand at fixed relative density and confining stress level could decrease by adding small amount of silts. On the other hand, for geometrically similar gradations (i.e. samples with similar coefficient of uniformity C_u, but with different D_{50}), the study by Nakata *et al.* (2001) on silica sand showed that the elastic stiffness is barely affected for as much as a five-fold increase in D_{50}. In the small-strain regime, Wichtmann & Triantafyllidis (2009) argued that shear modulus is independent of D_{50} based on their 163 resonant column tests on 25 quartz sands with different gradations. Regarding $\dot{B}_0$ and n, the influence of scaling on the viscous properties of rockfills is little known. Only a few creep experiments on rockfills have been reported in the literature (Oldecop & Alonso, 2002; Zhang *et al.*, 2017) and none of them has focused on the grain size effect. Oldecop & Alonso (2007) suggested that the long-term deformation of rockfills is intimately linked to their short-term behaviours. This can indeed be captured through the scaling of E_c, as a smaller yield surface creates a higher overstress for a given stress state and thus drives more viscoplastic straining (Figs 2(c) and 2(d)). Regarding the rest of the model parameters, Wood & Maeda (2008) found that gradation has a negligible influence on the critical stress ratio M. The slight variations of the grading index ϑ and breakage-plastic coupling angle ω with respect to D_{50} are also negligible compared to the changes in E_c (Zhang & Buscarnera, 2014). For the above reasons, the present authors consider that equation (11) is sufficient to capture the first-order scaling effects that are relevant to the settlement analysis conducted in the present study.

THE SHUIBUYA CFRD

The Shuibuya CFRD is currently the tallest dam of its kind in the world, representing the state of the art of dam

Downloaded by [UNIV OF ILLINOIS] on [05/02/20]. Copyright © ICE Publishing, all rights reserved.

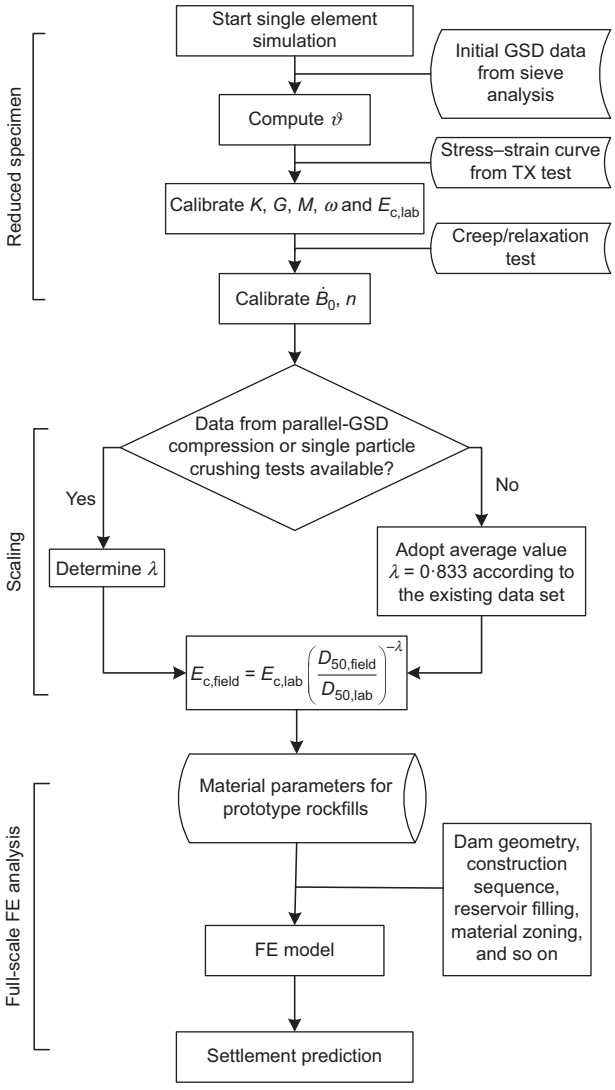

Fig. 3. Flow chart of breakage-mechanics-based settlement analysis of rockfill dams

engineering and construction technology for rockfill structures. A rich data set from element material testing to global settlement measurement is available through several technical papers and reports (Zhou *et al.*, 2011a, 2011b, 2016), thus offering a unique opportunity to validate new rockfill models and analyse methodologies.

The Shuibuya dam was built on the Qingjiang River in Badong city, Hubei Province, China (Fig. 4(a)). It is 233·2 m high and 675 m long across a U-shaped river valley (Fig. 4(b)). The maximum reservoir elevation is 400 m, with a water storage capacity of $4{\cdot}59 \times 10^9$ m^3. The crest is 12 m wide, installed with 5·2 m high L-shaped parapets. The slopes of both upstream and downstream dam are 1 : 1·4 (Fig. 4(c)). The dam sits on a foundation at 175·8 m elevation, characterised by multiple strata of Longtan shale, Maokou limestone and Qixia limestone from top to bottom. The river wash is mainly sandy gravel and also includes sandy boulder, sandy silt and silty clay phacoid. The typical zoning of the Shuibuya CFRD is shown in Fig. 4(c). It consists of: (*a*) $9{\cdot}45 \times 10^5$ m^3 silty sandstone; (*b*) $5{\cdot}5 \times 10^4$ m^3 clay; (*c*) $3{\cdot}84 \times 10^5$ m^3 cushion material produced from Qixia limestone; (*d*) $7{\cdot}21 \times 10^5$ m^3 transition material produced from excavated Qixia limestone; (*e*) $8{\cdot}25 \times 10^6$ m^3 primary rockfill made of Maokou limestone; (*f*) $4{\cdot}08 \times 10^6$ m^3 secondary rockfill made of a mixture of Qixia soft and hard limestone; and (*g*) $2{\cdot}22 \times 10^6$ m^3 downstream rockfill made of Qixia hard limestone and basalt. Laboratory tests have been conducted on primary and secondary rockfills. Triaxial compression, proportional loading and constant mean stress tests have been performed on reduced specimens under confining stresses from 0·2 MPa to 2·5 MPa. Creep tests have been also conducted for primary rockfills. The construction began in 2002 and was completed in 2006; then the reservoir was gradually filled over the period of October 2006 to November 2008. The settlement monitoring system of the dam includes 18 reference stations, 56 external surface settlement markers (at the abutment, the face slab and the downstream shell of the dam) and 70 internal displacement gauges distributed in three representative cross-sections (0 + 132 m, 0 + 212 m and 0 + 356 m). In order to monitor the settlement at the dam crest, seven measurement points (SL1 to SL7) were installed along the dam's longitudinal axis at an elevation of 405 m. Fig. 5 shows the layout of 38 extensometers at the maximum cross-section (0 + 2126 m) of the dam, a part of the internal settlement monitoring system (ISMS). The measured settlement together with the construction and filling records from 2004 to 2010 permits a comprehensive study of the deformation response of the dam subjected to combined gravitational and hydrostatic loads.

UMAT IMPLEMENTATION AND FE MODEL

The rate-dependent breakage model is implemented in a user subroutine 'UMAT' by way of an explicit error-controlled substepping algorithm adapted from Sloan (1987). A slight modification here is that Δt represents a finite increment in physical time instead of pseudo time that controls the loading progress for quasi-static models. Single-element tests are conducted to verify the implementation against a stand-alone constitutive driver. Fig. 6 compares the computed stress–strain curves and breakage evolution of drained triaxial compression tests under different strain rates using parameters calibrated for Virginia Beach sand. Perfect agreement between the two simulations is observed.

Parameters for the primary and secondary rockfills of the Shuibuya dam are calibrated and scaled through the procedure depicted in Fig. 3. Fig. 7 reports the gradation of the reduced and the prototype rockfills. The initial GSD of the reduced specimen is fitted by $F_0(x) = (x^{3-\beta} - D_{\min}^{3-\beta})/(D_{\max}^{3-\beta} - D_{\min}^{3-\beta})$ using $\beta = 2{\cdot}36$ and $D_{\min} = 0{\cdot}01$ mm and $D_{\max} = 60$ mm. The ultimate fractal GSD is described by $F_u(x) = (x^{3-\alpha} - D_{\min}^{3-\alpha})/(D_{\max}^{3-\alpha} - D_{\min}^{3-\alpha})$ with the same values of $D_{\max}$ and $D_{\min}$. Evidence from geological fault gouges (Sammis *et al.*, 1987), high-pressure experiments (Hardin, 1985; Coop *et al.*, 2004) and DEM simulations (Ben-Nun & Einav, 2010) showed that the ultimate fractal dimension α ranges between 2·6 and 2·7. In this study, $\alpha = 2{\cdot}7$ is selected. Supplying the above coefficients in the expression of the grading index (Einav, 2007a), a value of $\vartheta = 0{\cdot}42$ is obtained. The mechanical parameters are calibrated through triaxial compression tests (Fig. 8), which are conducted on fully saturated specimens with dry density 2·13 g/cm^3. Parameters K and G are obtained by matching the pre-yielding portion of the stress–strain curves; E_c, M and ω are determined according to the yielding and hardening responses. It is observed that the model captures well the stress–strain curves at different confining stresses, with some discrepancies on the volumetric response. This is due to the simple linear elasticity model adopted in this study and the lack of critical state concept in the current breakage model. Improvements can be made by adopting pressure-dependent elasticity (Nguyen & Einav, 2009) and employing

Downloaded by [UNIV OF ILLINOIS] on [05/02/20]. Copyright © ICE Publishing, all rights reserved.

(a)

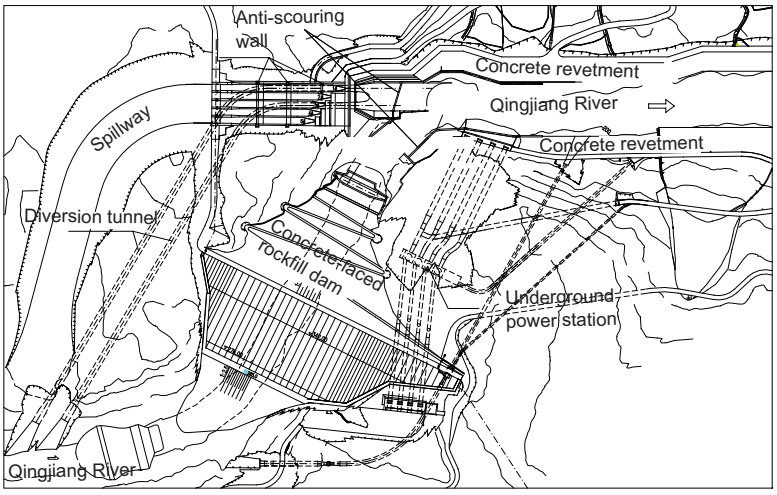

(b)

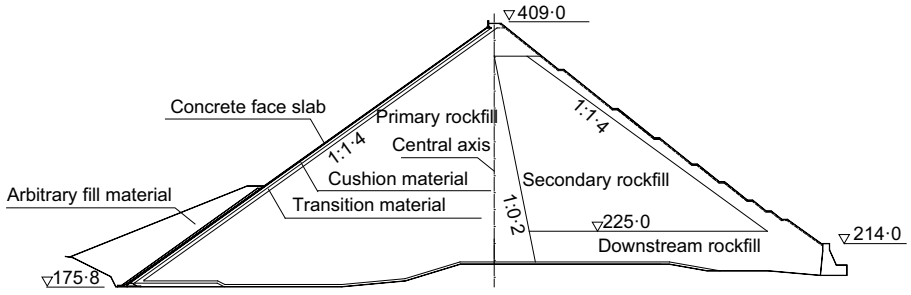

(c)

Fig. 4. (a) Top view; (b) layout; (c) zoning of the Shuibuya CFRD

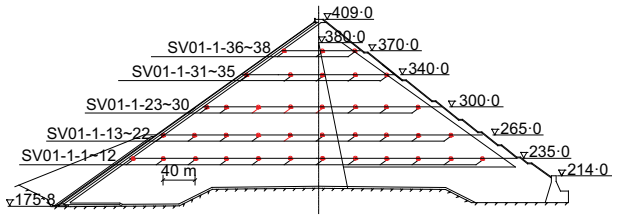

Fig. 5. Layout of ISMS at the maximum cross-section (0 + 212 m) of the Shuibuya CFRD (the numbering of sensors increases from left to right)

porosity as a state variable in the model (Tengattini *et al.*, 2016), which may be pursued in advanced breakage-based simulations.

All the tests presented in Fig. 8 were conducted under quasi-static condition (constant strain rate of 0·5%/min), and thus cannot be used to calibrate the viscosity parameters. Instead, $\dot{B}_0$ and n are determined using data from the triaxial creep tests on the primary rockfill (Cheng & Ding, 2004) (Fig. 9). Two sets of data are referenced here, differing in their confining stresses (2·7 MPa, 1·8 MPa) and the level of axial strains (6·2%, 5·4%) prior to the creep test. The obtained corrosion index $n = 6$ is slightly lower than the typical range of n for quartz rocks (Atkinson, 1982) (meaning stronger rate sensitivity according to Fig. 2(a)). This may be due to the use of a fully saturated test condition and the water-sensitive nature of limestones. The same viscous properties are assumed for the secondary rockfills due to the lack of creep test data. Parametric analysis has revealed that $a \pm 50\%$ variation of $\dot{B}_0$ and n for the secondary rockfill has negligible effects on the simulation

Downloaded by [UNIV OF ILLINOIS] on [05/02/20]. Copyright © ICE Publishing, all rights reserved.

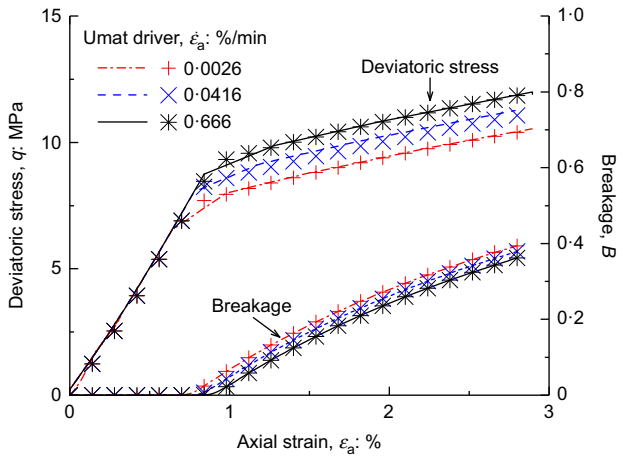

Fig. 6. The predicted stress–strain and breakage curves of Virginia Beach sand from a stand-alone constitutive driver and the implemented Umat by way of single-element simulation

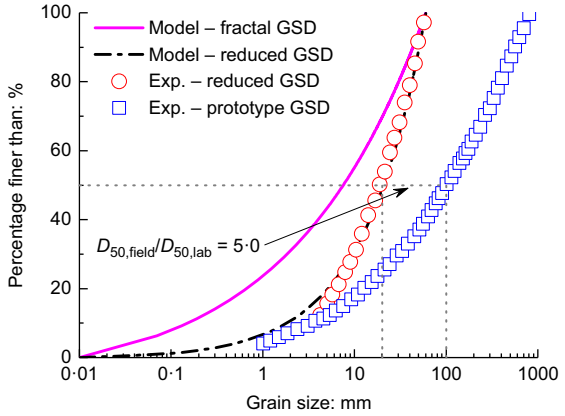

Fig. 7. Grain size distribution of the reduced and the prototype rockfills and model calibration

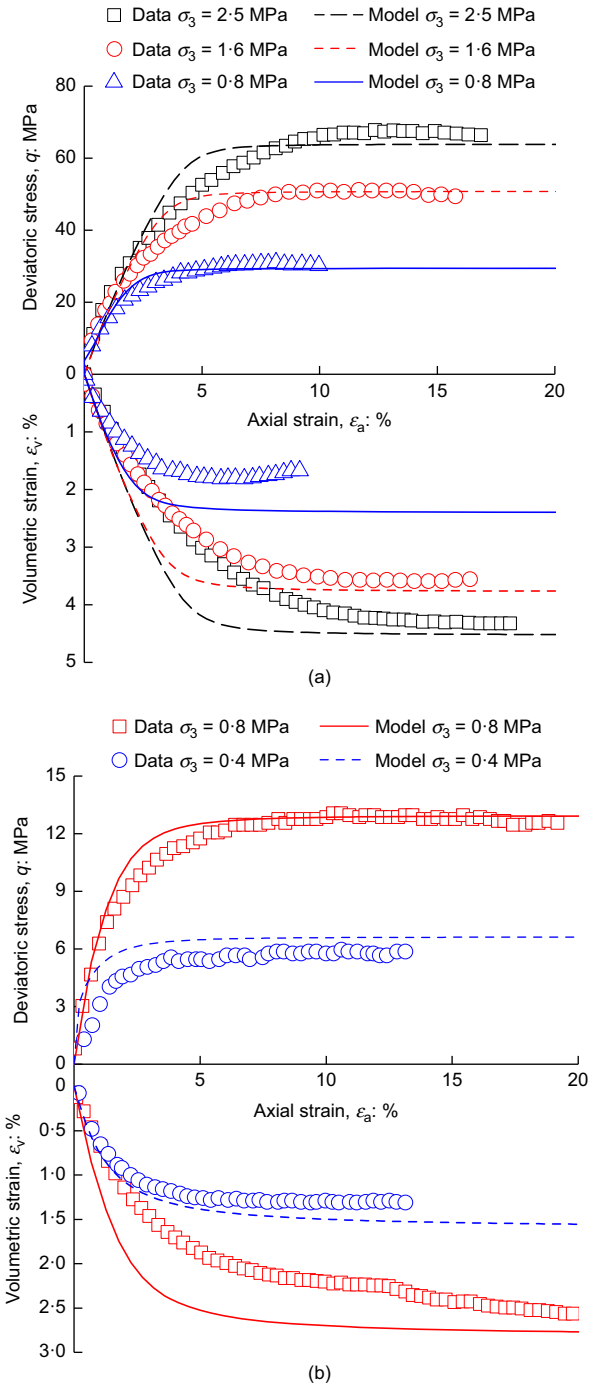

Fig. 8. Model compared with data of triaxial tests on: (a) primary rockfill; (b) secondary rockfill

results. Finally, the calibrated critical breakage energy $E_{c,lab}$ values are upscaled to represent the crushability of the prototype rockfills. From Fig. 7, it reads $D_{50,field}/D_{50,lab} = 5{\cdot}0$. Substituting this value and the scaling parameter $\lambda = 0{\cdot}833$ into equation (11), $E_{c,field}$ can be determined for the primary and secondary rockfills. Parameters determined through the above procedure are listed in Table 3. The downstream rockfill has very similar properties as the primary rockfill (Zhou *et al.*, 2011b), and thus is assigned with the same parameters. The cushion and the transition materials are expected to have minimum impact on the internal settlement given their small filling volume. Therefore, they are modelled by the Duncan–Chang E-B model (Duncan & Chang, 1970) with the same parameters reported in Zhou *et al.* (2011b).

Figure 10 presents the FE model for the Shuibuya dam considering the construction and impoundment sequence. The construction stage is simulated by 42 steps following exactly the construction timeline of the project. The simulation of these steps is realised by sequentially adding element sets and gradually increasing the weight of each layer to achieve full gravitational load at the end of that construction period. An average density of 2150 kg/m^3 is assigned to the rockfills. Since the duration of each ramp loading is consistent with the reported construction progress, the onset of creep is automatically determined by the constitutive model under realistic construction stress paths. The hydrostatic load is discretised and applied on the upstream surface in 58 steps, in accordance with the reservoir level records, to reflect the impact of impoundment and water level fluctuation during 2006~2010. The interfaces jointing the dam and the adjacent valleys and the bedrocks are prescribed as fixed displacement boundaries. In summary, the three-dimensional FE model contains 11 958 eight-node elements, 100 loading steps and five rockfill materials. It is worth mentioning that the moisture-sensitive behaviour of rockfills is not considered in the current model. The water level on the upstream and downstream side of the dam is quite steady and no extreme rainfall events or sudden rise of the water level has occurred during the operation of the dam. Therefore, this study has handled the water weakening effect in an intrinsic manner by calibrating the model against test results from saturated rockfill specimens (Fig. 8). This permits a first-order mechanical

Downloaded by [UNIV OF ILLINOIS] on [05/02/20]. Copyright © ICE Publishing, all rights reserved.

analysis before taking environmental factors into consideration. The moisture effect has been recently incorporated in the breakage mechanics theory (Zhang & Buscarnera, 2018), which will be integrated with the proposed workflow for future studies of rockfill dams under fluctuating hydrological conditions.

PREDICTION RESULTS

The predicted results from the FE analysis and the settlement data from the ISMS system are compared by way of two types of plot. The first type compares the settlement histories at different locations with those extracted from the output database of the FE simulation, highlighting the temporal evolution of deformation in responding to loading sequences. The second type compares the settlement contours at different time points, visualising the spatial pattern of deformation within the dam.

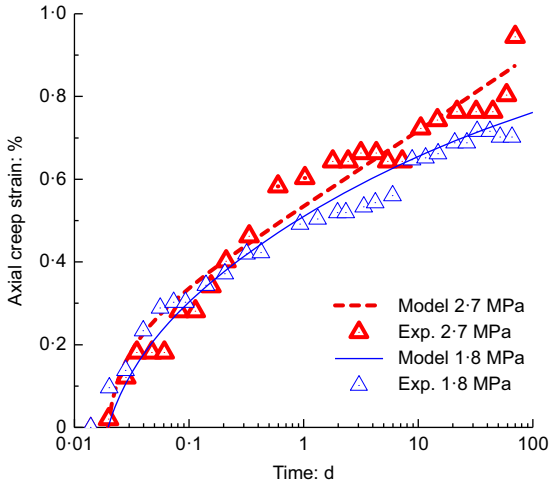

Fig. 9. Creep curves of the primary rockfill of the Shuibuya CFRD. Data from Cheng & Ding (2004)

Settlement history plots

The settlement observed at the dam crest reflects the accumulated compression of the dam body since the completion of construction (Gikas & Sakellariou, 2008). It is a good indicator of the differential settlement along the dam's length and is important for structural integrity evaluations. Figs 11(a) and 11(c) present the recorded settlement history and distribution from seven surface markers on the dam crest, and Figs 11(b) and 11(d) report the predicted results from the FE analysis.

Comparing Figs 11(a) and 11(b), it is observed that the predicted crest settlement agrees well with monitoring data prior to the full impoundment in August 2007. Upon reaching the maximum reservoir level, the computed settlement curves begin to oscillate and result in an underestimated overall crest settlement. These oscillations are associated with the recovery of elastic strain caused by the partial release of the reservoir after peak storage and seasonal fluctuations of the reservoir level. For this reason, the accumulated creep strain under sustained water loading is offset by elastic rebounding, leading to the approximately constant crest settlement after August 2007. This may be explained by the lack of plastic deformation mechanisms associated with cyclic loading paths. The upstream rockfills near the top of

Table 3. Mechanical parameters for the primary, secondary and downstream rockfill of the Shuibuya CFRD

Definition of parameter	Symbol	Units	Primary rockfill/downstream rockfill	Secondary rockfill
Grading index	ϑ		0·42	0·42
Bulk modulus	K	MPa	100	56
Shear modulus	G	MPa	150	80
Critical stress ratio	M		1·65	1·05
Breakage-plasticity coupling angle	ω	deg	30	40
Reference breakage growth rate	$\dot{B}_0$	$1/s$	0·001	0·001
Corrosion index	n		6	6
Scaling coefficient	λ		0·833	0·833
Critical breakage energy for the reduced specimens	$E_{c,lab}$	MPa	$2{\cdot}0 \times 10^{-3}$	$1{\cdot}8 \times 10^{-3}$
Critical breakage energy for the prototype rockfill	$E_{c,field}$	MPa	$5{\cdot}2 \times 10^{-4}$	$4{\cdot}7 \times 10^{-4}$

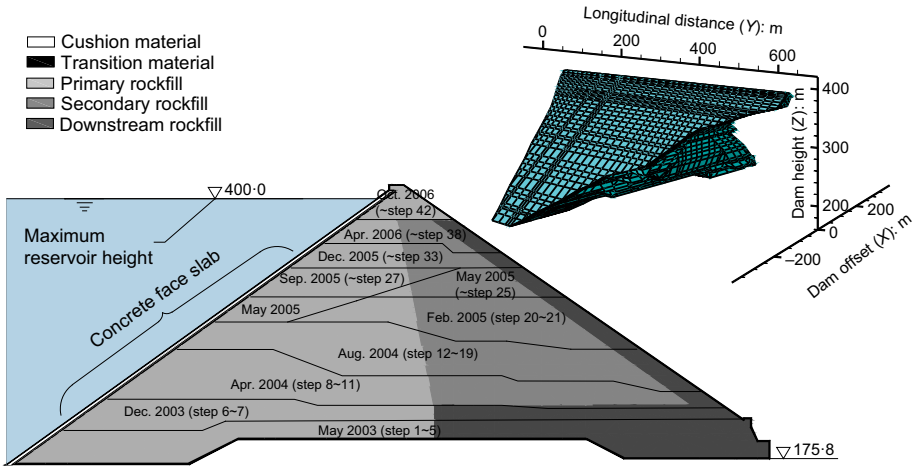

Fig. 10. FE mesh of the Shuibuya CFRD

Downloaded by [UNIV OF ILLINOIS] on [05/02/20]. Copyright © ICE Publishing, all rights reserved.

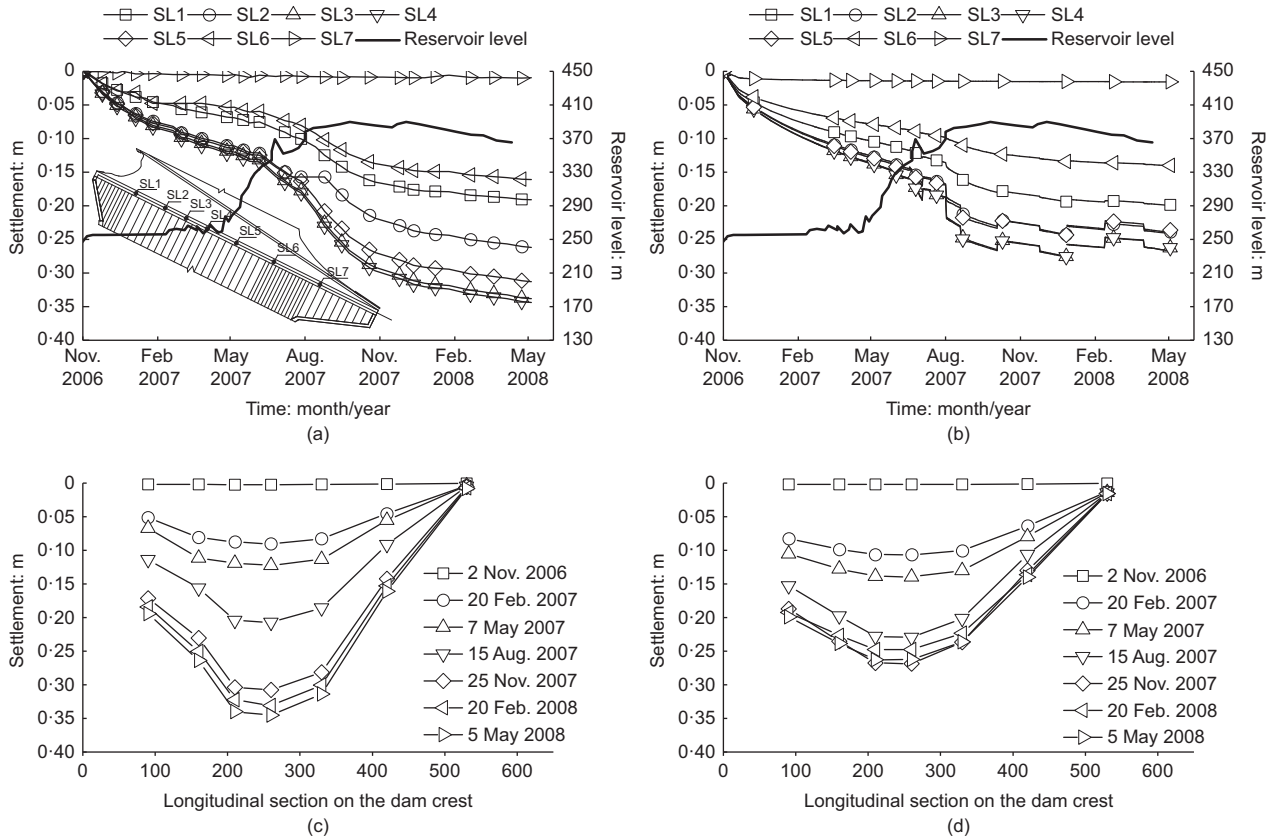

Fig. 11. The measured: (a) settlement history; (c) settlement profile along the dam crest from November 2006 to May 2008. (b) and (d) are the corresponding predictions from the FE analysis

the dam have relatively low overburden stress, thus fluctuation of the reservoir level will induce loading cycles of large magnitude that can plastically compact the rockfills. Modelling this behaviour requires the extension of breakage models with hypoplasticity features, as recently discussed by Einav (2012) and Das & Bajpai (2017). It is worth noting that the effect of cyclic degradation is much less important for rockfills at greater depths in the dam, as the magnitudes of cyclic loading become negligible compared to the overburden stresses. This will be soon confirmed by the lack of oscillations in the computed settlement curves inside the dam. The saddle-shaped settlement profile across the crest shown in Fig. 11(c) is successfully captured by the FE analysis (Fig. 11(d)). The predicted profiles before August 2007 agree particularly well with the measured ones, suggesting a good performance of the model in representing the monotonic behaviour of rockfills. Again, the overall crest settlement after August 2007 is under-predicted due to the cyclic effect.

Among the three monitored cross-sections, the 0 + 212 m section is selected as the focus of comparisons as it is the maximum cross-section of the dam and has installed more sensors than the other two. Figs 12(a) and 12(b) report the measured and predicted settlement histories at elevation of 235 m, respectively. Several characteristic trends are successfully captured by the FE model: (*a*) settlement near the centre of the dam (reported by SV01-1-6 to SV01-1-10) develops faster than that near the upstream concrete face (SV01-1-1 to SV01-1-5) during construction, whereas the trend is reversed during the impoundment stage; (*b*) settlement continues to develop after the dam is filled to maximum capacity (August 2007). The first trend can be explained by the fact that the rockfill near the upstream surface is only subjected to a small portion of overburden pressures during construction, but serves as the main load-bearing material upon reservoir filling, thus responding more sensitively to impoundment. The second trend is mainly attributed to the creep behaviour of the rockfill materials. Fig. 13 presents the measured and predicted settlement for elevation 300 m. Again, the predicted maximum settlements at different elevations agree remarkably well with the recorded values. Such a level of agreement is given by the forward procedure described in Fig. 3 rather than from back-analysis.

In the operation stage, slightly higher creep rates (0·05 m/year) are observed for monitoring points SV01-1-6 to SV01-1-8 than the computed ones (0·02 m/year). These points are located at the lowest elevation monitored (235 m), near the central line of the dam. Noticing such high creep rates disappeared at higher elevations (300 m, Fig. 13), it is inferred that the accelerated creep is caused by possible seepage flow with the low phreatic line near the dam foundation. This can cause high moisture content or even full saturation for rockfills at low elevations and accelerate their degradation. A fully coupled hydromechanical analysis with moisture-dependent breakage model may capture these subtle differences in future studies. Another observation is that, among the predicted settlement curves during the operation stage, those extracted at locations near the upstream surface of the dam (SV01-1-1 to SV01-1-5) exhibit similar fluctuations to the crest settlement curves, whereas those near the centre of the dam (SV01-1-6 to SV01-1-10) are relatively insensitive to the fluctuation of the reservoir level. This is consistent with the previous conclusion that the cyclic loading induced by changes of water level is less significant for internal rockfills away from the concrete slabs. The predicted maximum settlement at this elevation is in perfect agreement with the observed value (1·3 m). However, such magnitude is predicted to occur at location SV01-1-9 instead of SV01-1-7,

Downloaded by [UNIV OF ILLINOIS] on [05/02/20]. Copyright © ICE Publishing, all rights reserved.

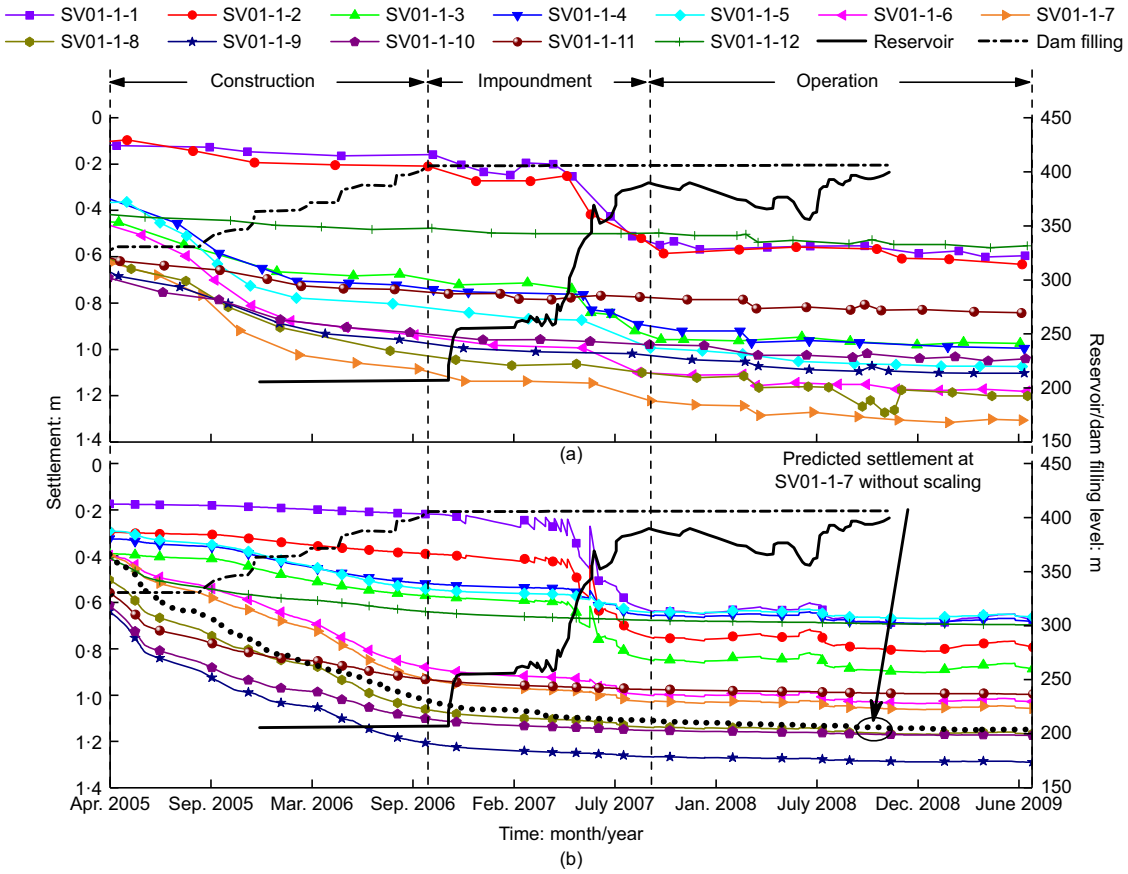

Fig. 12. (a) Measured; (b) predicted settlement at the elevation of 235 m in the 0 + 212 m cross-section

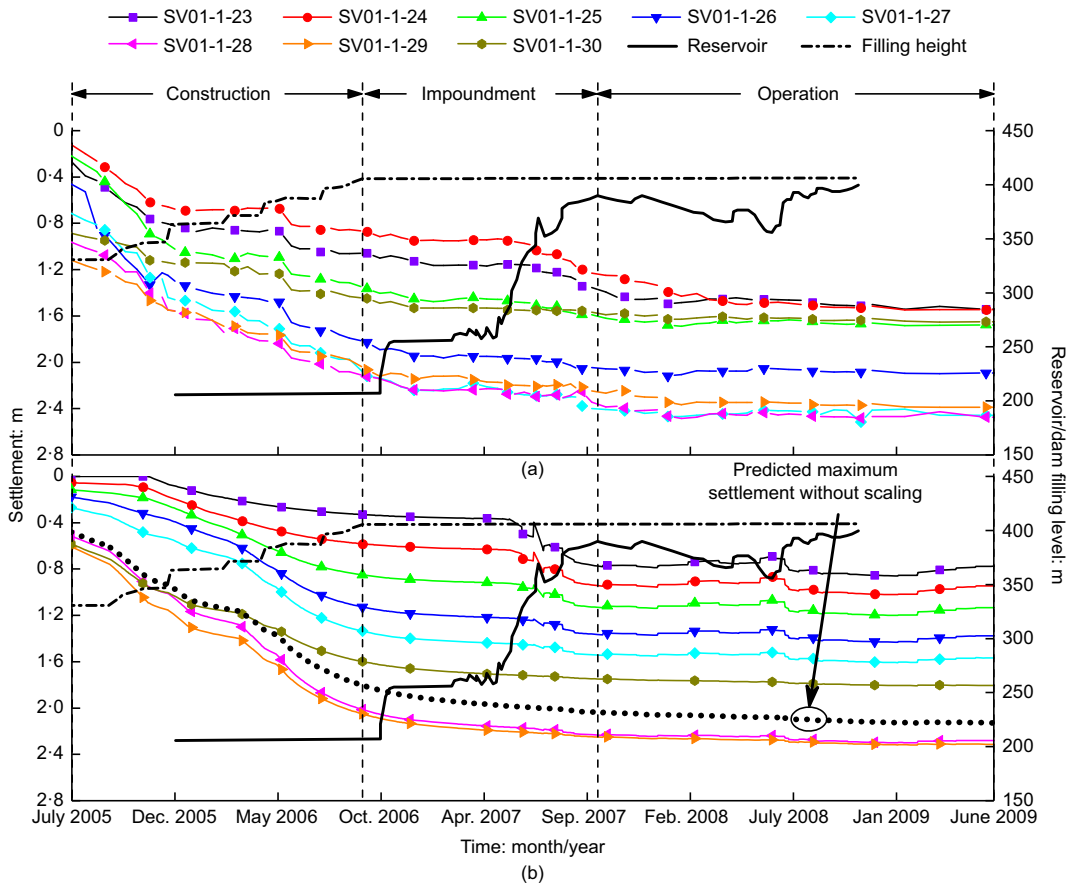

Fig. 13. (a) Measured; (b) predicted settlement at the elevation of 300 m in the 0 + 212 m cross-section

Downloaded by [UNIV OF ILLINOIS] on [05/02/20]. Copyright © ICE Publishing, all rights reserved.

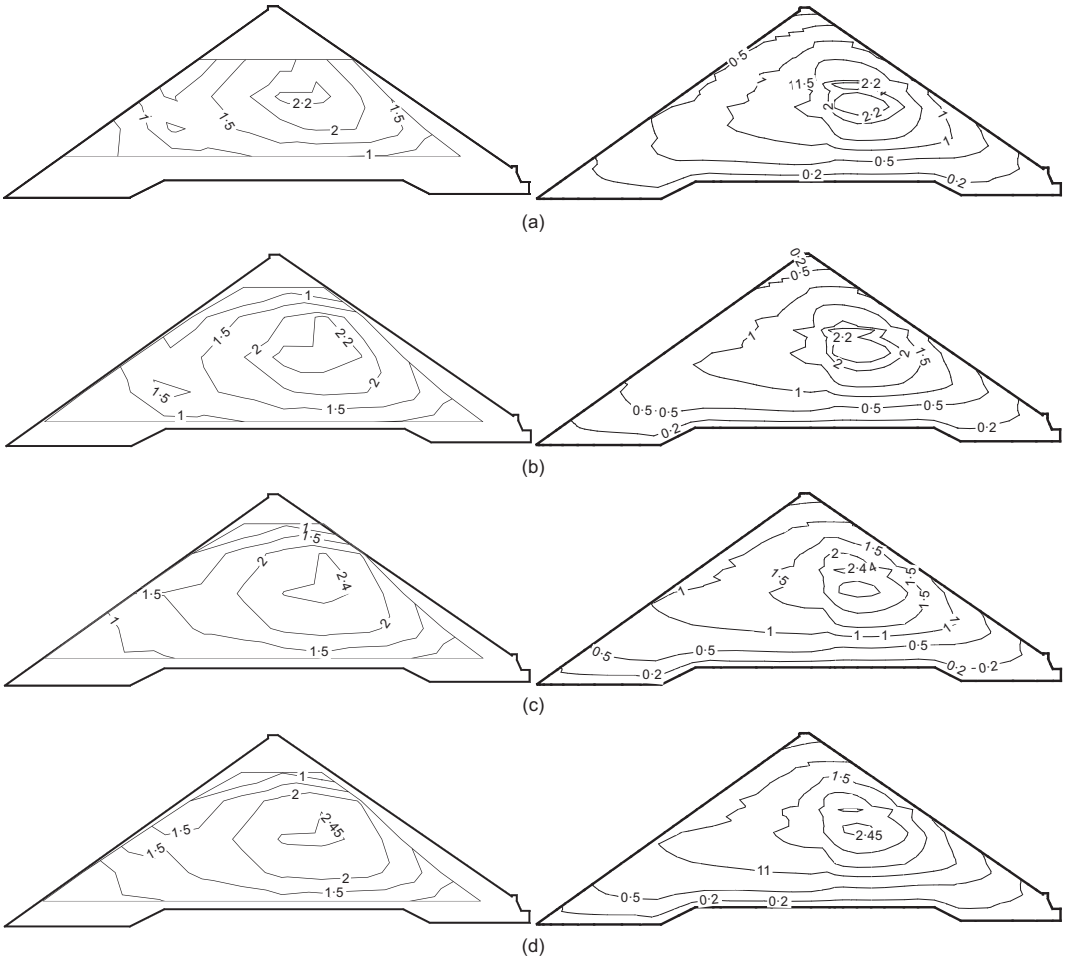

Fig. 14. Measured (left) compared with predicted (right) settlement at the 0 + 212 m cross-section in: (a) December 2006; (b) July 2007; (c) November 2008; (d) April 2010

as shown in Fig. 12(a). This indicates a slight discrepancy in the predicted spatial distribution of settlements, which is more conveniently discussed using contour plots in the next section.

Settlement contour at different time points

Figure 14 reports the settlement contours for the 0 + 212 m section from the end of construction (Fig. 14(a)) to the latest monitoring record (Fig. 14(d)). For each plot, the contour on the left presents the data measured from the ISMS and that on the right presents the predictions of the FE model. The region beyond the coverage of ISMS instrumentation is left blank. In general, a satisfactory agreement is observed. The FE model successfully captures that the maximum settlement zone locates near the downstream side of the dam, given the relatively low strength and stiffness of the secondary rockfill. The predicted contours locate slightly to the right of the measured ones, which explains the mismatch on the sensors reporting the maximum settlement discussed in the previous section. The maximum settlement increased from 2·2 m to 2·45 m over 4 years, which is also captured by the FE model. All the contours from FE simulations contain some rough edges. They are caused by the discretisation of the construction steps and consequently different total time allowed for each of the rockfill layers to develop creep strains. In summary, these agreements support the predictive capability of the proposed constitutive model and the upscaling strategy for the settlement assessment of large rockfill structures.

DISCUSSION

Grain size effect

A separate FE simulation is conducted using unscaled parameters (i.e. $E_{c,lab}$ instead of $E_{c,field}$). The predicted maximum settlement at elevations 235 m and 300 m are plotted together with the baseline results in Figs 12(b) and 13(b), respectively. Fig. 15 reports the computed settlement contour in April 2010 using scaled (solid lines) and unscaled (dash-dotted lines) values of E_c. As expected, the use of $E_{c,lab}$ would substantially underestimate the overall settlement by an average of 14%. This implies that neglecting the scaling effect in large CFRDs can promote unconservative designs of the concrete slabs and crest highways.

Time effect

The contribution of creep on the total deformation can be separated by turning off the rate-dependent feature of the

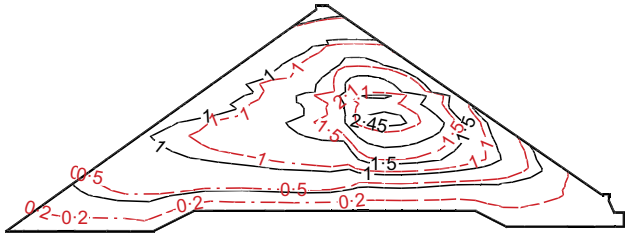

Fig. 15. Grain size effect on the predicted settlement contour at the 0 + 212 m cross-section in April 2010

Downloaded by [UNIV OF ILLINOIS] on [05/02/20]. Copyright © ICE Publishing, all rights reserved.

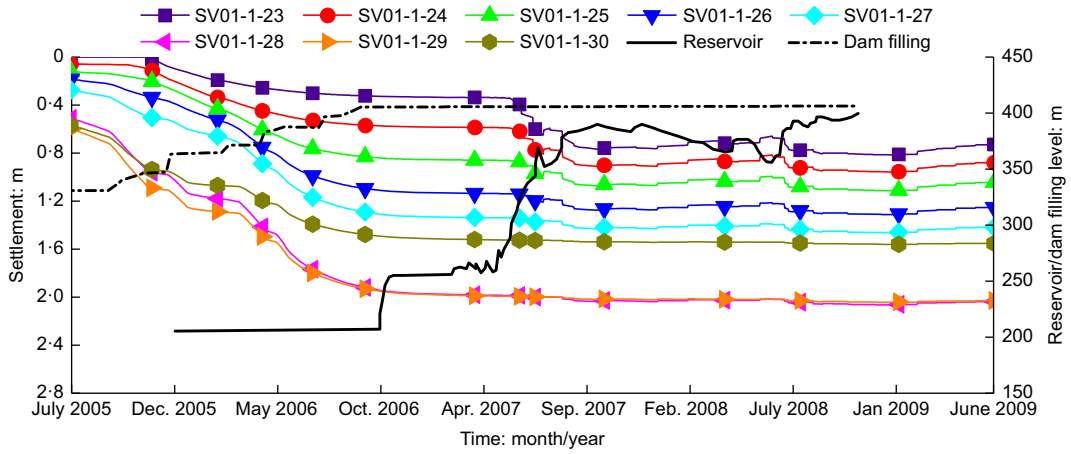

Fig. 16. Predicted settlement without creep at the 0 + 212 m cross-section on elevation of 300 m

model. This can be achieved by increasing the value of either n or $\dot{B}_0$ – that is to create instantaneous inelastic flow even under small overstress according to equations (6) and (7). It is found that the use of $n = 50$ is sufficient to suppress the time effect in this study. The predicted settlement histories and contours are shown in Figs 16 and 17. Comparing Fig. 16 with Fig. 13(a), it is observed that the settlement develops quite similarly at the construction stage, but diverts during the impoundment and the operation phases. In particular, settlement has almost ceased after the maximum reservoir level is reached according to this simulation. The predicted maximum settlement 2·0 m is 18% lower than the field observations. In comparison to the settlement contours with creep (black solid lines in Fig. 17), the predictions without creep (dash-dotted lines) will underestimate the maximum settlement as well as alter the global deformation pattern. For example, the settlement level near the centre of the dam is significantly reduced, whereas near the boundary of the dam it is not much affected.

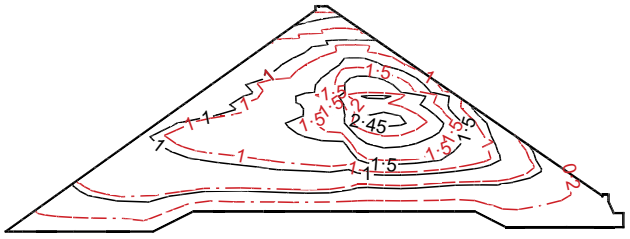

Fig. 17. Time effect on the predicted settlement contour in the 0 + 212 m cross-section in April 2010

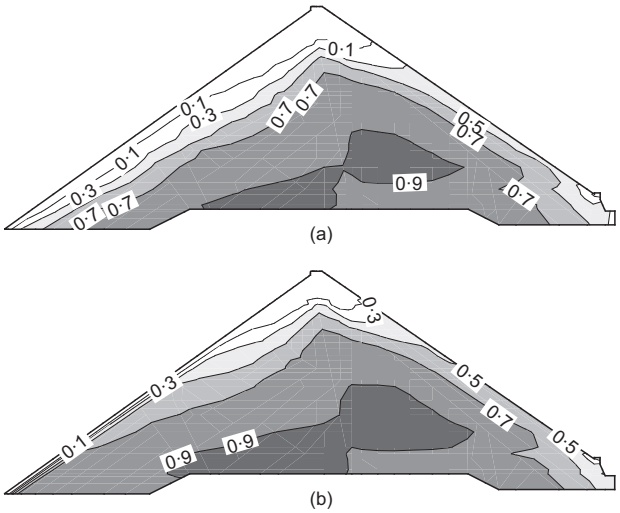

Fig. 18. Breakage contour of Shuibuya CFRD in: (a) October 2006; (b) April 2010

Breakage evolution

A unique feature of breakage mechanics-based deformation analysis is to track the microstructural degradation of rockfills at any spatial and temporal points by way of the breakage index B. Figs 18(a) and 18(b) report the predicted breakage contours immediately after construction and after 3 years of operation. It is obvious that rockfills located at the lower part, near the centre of the dam, experience the most severe breakage due to the self-weight of the dam. Less breakage is predicted for rockfills near the faces and the crest of the dam. Over 3 years of operation, the breakage contours are expanded, governed by the delayed breakage evolution law (equation (6)). It is believed, however, that the overall magnitude of the breakage index inside the dam is over-predicted. A value of $B = 0{\cdot}9$ suggests that the rockfill is almost completely crushed to its ultimate fractal state, which is not likely for the stress levels encountered in this dam (0·8–2·4 MPa). Such over-prediction is due to the idealised breakage evolution law in the current model. Under isotropic compression, this law can be written as

$$E_B = \frac{E_c}{(1-B)^2} \tag{12}$$

through which a B–p relation can be obtained by substituting equation (4) and replacing ε_v with p using the elastic relation. Fig. 19 plots this relation extracted from a lower central node in the FE model together with the experimental data from Pyramid dam rockfills (Yin *et al.*, 2016). Apparently, the predicted B evolves towards unity at a rate that is much faster as compared to experimental observations. This indicates a need to develop a more accurate and flexible breakage evolution law for breakage models.

CONCLUSIONS

A procedure has been proposed for the settlement analysis of rockfill dams that can account for the time- and scale-dependent behaviours of rockfills. The new methodology integrates the rate-dependent breakage mechanics theory and the scaling law for the critical breakage energy of the

Downloaded by [UNIV OF ILLINOIS] on [05/02/20]. Copyright © ICE Publishing, all rights reserved.

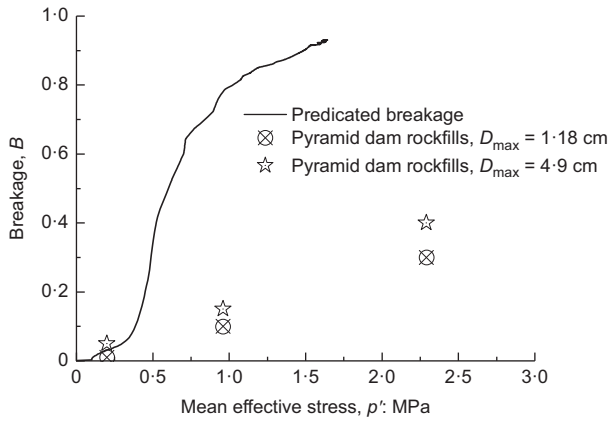

Fig. 19. Predicted breakage evolution near the centre of Shuibuya dam and measured breakage values for Pyramid dam rockfill undergoing triaxial shearing to critical state (data from Yin *et al.* (2016))

granular matrix. The procedure requires eight model parameters and one scaling parameter, which can be readily calibrated from standard laboratory testing programmes. The predictive performance of this framework is validated through a comprehensive case study on the Shuibuya CFRD. The main observations are: (*a*) the spatial distribution and temporal evolution of the settlement of the dam are well captured by the model using scaled parameters; (*b*) disabling the scaling- and the time-dependent features of the model will result in an average of 14% and 18% under-prediction of the dam settlement, respectively. These findings suggest that the incorporation of grain breakage and the associated microscale processes is the key step towards improved deformation predictions of rockfill structures. Compared to the usual E-B model-based FE analysis, the proposed method has the following advantages: (*a*) the extrapolation of test results from reduced specimens to the properties of prototype rockfills can be performed on a rational basis using analytical tools developed from particle-scale mechanics; (*b*) the model tracks the evolution of the GSD during the course of the loading process, allowing for explicit modelling of the time and scale effect associated with grain fracturing; (*c*) the model parameters have clear physical meanings and straightforward calibration procedures, and thus can be easily implemented for practical applications. The proposed framework is susceptible to numerous generalisations and enhancements. Relative humidity can be introduced as an additional degree of freedom in the FE analysis in combination with a moisture-dependent breakage model (e.g. Zhang & Buscarnera, 2018). This is necessary for applications involving strong coupling with a hydrological condition such as clay core rockfill dams. Cyclic degradation can be modelled by introducing dissipation mechanisms within the yield surface (e.g. Das & Bajpai, 2017), which allows for more accurate description of rockfills near the upstream. Finally, the current model over-predicts the extent of breakage inside the dam, calling for more accurate evolution laws specific to rockfill materials. In summary, this study provides an important first step towards a fully coupled hydromechanical framework for deformation analysis of rockfill structures, taking into account the effects of loading cycles, flooding, rainfall infiltration, particle breakage, creep and grain size scaling.

ACKNOWLEDGEMENT

Yida Zhang wishes to express thanks for the start-up fund provided by the Department of Civil, Environmental and Architectural Engineering at the University of Colorado Boulder, USA.

NOTATION

B	breakage
$\dot{B}_0$	reference breakage growth rate
D_{min}, D_{max}, D_{50}	minimum, maximum and median grain size
$D_{50,lab}$, $D_{50,field}$	median grain size for reduced and prototype rockfills, respectively
d_p	grain size
E_B, E_c	breakage energy and its critical value at the onset of crushing
$E_{c,lab}$, $E_{c,field}$	critical breakage energy for reduced and prototype rockfills, respectively
E_{pc}	particle fracture energy
F_0	initial cumulative grain size distribution
G	shear modulus
K	bulk modulus
M	stress ratio at frictional failure
n	stress corrosion index
P	compressive load
p, q	mean and deviatoric stress
$\tilde{p}$, $\tilde{q}$	mean and deviatoric stress in dissipative space
p'	effective mean stress
w	flow potential
δ_{ij}	Kronecker delta
ε_{ij}, e_{ij}	strain tensor and its deviator
ε_v, ε_s	volumetric and deviatoric strain
ς_{pB}, y_{pB}	breakage-plastic overstress function and yield surface
$\tilde{\varsigma}_{pB}$, $\tilde{y}_{pB}$	breakage-plastic overstress function and yield surface in dissipative stress space
ϑ	grading index
λ	power law coefficient
ξ	upscaling coefficient
σ_{ij}, s_{ij}	stress tensor and its deviator
$\tilde{\sigma}_{ij}$, $\tilde{E}_B$	dissipative stresses
ϕ	initial porosity
Ψ	Helmholtz free energy
ω	plastic-breakage coupling angle

REFERENCES

Alonso, E., Olivella, S., Soriano, A., Pinyol, N. & Esteban, F. (2011). Modelling the response of Lechago earth and rockfill dam. *Géotechnique* **61**, No. 5, 387–407, https://doi.org/10.1680/geot.SIP11.P.013.

Alonso, E. E., Romero, E. E. & Ortega, E. (2016). Yielding of rockfill in relative humidity-controlled triaxial experiments. *Acta Geotechnica* **11**, No. 3, 455–477.

Atkinson, B. K. (1982). Subcritical crack propagation in rocks: theory, experimental results and applications. *J. Struct. Geol.* **4**, No. 1, 41–56.

Ben-Nun, O. & Einav, I. (2010). The role of self-organization during confined comminution of granular materials. *Phil. Trans. R. Soc. Lond. A: Math., Phys. Engng Sci.* **368**, No. 1910, 231–247.

Chávez, C., Romero, E. & Alonso, E. E. (2009). A rockfill triaxial cell with suction control. *Geotech. Testing J.* **32**, No. 3, GTJ101590.

Cheng, Z. L. & Ding, H. S. (2004). Creep test for rockfill. *Chin. J. Geotech. Engng – Chin. Edn* **26**, 473–476.

Cil, M. B. & Buscarnera, G. (2016). DEM assessment of scaling laws capturing the grain size dependence of yielding in granular soils. *Granular Matter* **18**, No. 3, 36.

Collins, I. & Houlsby, G. (1997). Application of thermomechanical principles to the modelling of geotechnical materials. *Proc. R. Soc. Lond. A: Math., Phys. Engng Sci.* **453**, No. 1964, 1975–2001.

Coop, M., Sorensen, K., Freitas, T. B. & Georgoutsos, G. (2004). Particle breakage during shearing of a carbonate sand. *Géotechnique* **54**, No. 3, 157–164, https://doi.org/10.1680/geot.2004.54.3.157.

Downloaded by [UNIV OF ILLINOIS] on [05/02/20]. Copyright © ICE Publishing, all rights reserved.

Das, A. & Bajpai, P. K. (2017). A hypo-plastic approach for evaluating railway ballast degradation. *Acta Geotechnica*, https://doi.org/10.1007/s11440-017-0584-7.

Duncan, J. M. & Chang, C. Y. (1970). Nonlinear analysis of stress and strain in soils. *J. Soil Mech. Found. Div.* **96**, No. 5, 1629–1653.

Einav, I. (2007a). Breakage mechanics – Part I: theory. *J. Mech. Phys. Solids* **55**, No. 6, 1274–1297.

Einav, I. (2007b). Breakage mechanics – Part II: modelling granular materials. *J. Mech. Phys. Solids* **55**, No. 6, 1298–1320.

Einav, I. (2012). The unification of hypo-plastic and elasto-plastic theories. *Int. J. Solids Structs* **49**, No. 11, 1305–1315.

Gikas, V. & Sakellariou, M. (2008). Settlement analysis of the Mornos earth dam (Greece): evidence from numerical modeling and geodetic monitoring. *Engng Structs* **30**, No. 11, 3074–3081.

Hardin, B. O. (1985). Crushing of soil particles. *J. Geotech. Engng* **111**, No. 10, 1177–1192.

Houlsby, G. T. (2014). Dissipation rate functions, pseudopotentials, potentials and yield surfaces. In *Beyond the second law: entropy production and non-equilibrium systems* (eds R. C. Dewar, C. H. Lineweaver, R. K. Niven and K. Regenauer-Lieb), pp. 73–95. Berlin/Heidelberg, Germany: Springer.

Houlsby, G. T. & Puzrin, A. M. (2006). *Principles of hyperplasticity: an approach to plasticity theory based on thermodynamic principles*. London, UK: Springer.

Marachi, N. D., Chan, C. K. & Seed, H. B. (1972). Evaluation of properties of rockfill materials. *J. Soil Mech. Found. Div.* **98**, No. SM1, 95–114.

Marsal, R. J. (1967). Large-scale testing of rockfill materials. *J. Soil Mech. Found. Div.* **93**, No. 2, 27–43.

Marsal, R. J. (1973). *Mechanical properties of rockfill*. Hoboken, NJ, USA: John Wiley and Sons, Inc.

Nakata, Y., Kato, Y., Hyodo, M., Hyde, A. F. & Murata, H. (2001). One-dimensional compression behaviour of uniformly graded sand related to single particle crushing strength. *Soils Found.* **41**, No. 2, 39–51.

Naylor, D., Maranha Das Neves, E., Mattar, D. & Veiga Pinto, A. (1986). Prediction of construction performance of Beliche Dam. *Géotechnique* **36**, No. 3, 359–376, https://doi.org/10.1680/geot.1986.36.3.359.

Nguyen, G. D. & Einav, I. (2009). The energetics of cataclasis based on breakage mechanics. *Pure Appl. Geophys.* **166**, No. 10–11, 1693–1724.

Oldecop, L. & Alonso, E. (2002). Fundamentals of rockfill time-dependent behaviour. In *Unsaturated soils* (eds J. F. T. Juca, T. M. P. de Campos and F. A. M. Marinho), vol. 2, pp. 793–798. Lisse, the Netherlands: Swets and Zeitlinger.

Oldecop, L. A. & Alonso, E. (2007). Theoretical investigation of the time-dependent behaviour of rockfill. *Géotechnique* **57**, No. 3, 289–301, https://doi.org/10.1680/geot.2007.57.3.289.

Ovalle, C., Frossard, E., Dano, C., Hu, W., Maiolino, S. & Hicher, P. Y. (2014). The effect of size on the strength of coarse rock aggregates and large rockfill samples through experimental data. *Acta Mechanica* **225**, No. 8, 2199.

Pramthawee, P., Jongpradist, P. & Sukkarak, R. (2017). Integration of creep into a modified hardening soil model for time-dependent analysis of a high rockfill dam. *Comput. Geotech.* **91**, 104–116.

Ramon, A., Alonso, E. & Romero, E. (2008). Grain size effects on rockfill constitutive behaviour. In *Proceedings of the 1st European conference on unsaturated soils* (eds D. G. Toll, C. E. Augarde, D. Gallipoli and S. J. Wheeler), pp. 341–347. London, UK: Taylor & Francis.

Salgado, R., Bandini, P. & Karim, A. (2000). Shear strength and stiffness of silty sand. *J. Geotech. Geoenv. Engng* **126**, No. 5, 451–462.

Sammis, C., King, G. & Biegel, R. (1987). The kinematics of gouge deformation. *Pure Appl. Geophys.* **125**, No. 5, 777–812.

Sloan, S. W. (1987). Substepping schemes for the numerical integration of elastoplastic stress–strain relations. *Int. J. Numer. Methods Engng* **24**, No. 5, 893–911.

Sohn, C., Zhang, Y. D., Cil, M. & Buscarnera, G. (2017). Experimental assessment of continuum breakage models accounting for mechanical interactions at particle contacts. *Granular Matter* **19**, No. 4, article 67.

Tapias, M., Alonso, E. & Gili, J. (2015). A particle model for rockfill behaviour. *Géotechnique* **65**, No. 12, 975–994, https://doi.org/10.1680/jgeot.14.P.170.

Tengattini, A., Das, A. & Einav, I. (2016). A constitutive modelling framework predicting critical state in sand undergoing crushing and dilation. *Géotechnique* **66**, No. 9, 695–710, https://doi.org/10.1680/jgeot.14.P.164.

Varadarajan, A., Sharma, K., Venkatachalam, K. & Gupta, A. (2003). Testing and modeling two rockfill materials. *J. Geotech. Geoenviron. Engng* **129**, No. 3, 206–218.

Wen, L., Chai, J., Xu, Z., Qin, Y. & Li, Y. (2017). Monitoring and numerical analysis of behaviour of Miaojiaba concrete-face rockfill dam built on river gravel foundation in China. *Comput. Geotech.* **85**, 230–248.

Wichtmann, T. & Triantafyllidis, T. (2009). Influence of the grain-size distribution curve of quartz sand on the small strain shear modulus G max. *J. Geotech. Geoenv. Engng* **135**, No. 10, 1404–1418.

Wood, D. M. & Maeda, K. (2008). Changing grading of soil: effect on critical states. *Acta Geotechnica* **3**, No. 1, 3.

Yin, Z. Y., Hicher, P. Y., Dano, C. & Jin, Y. F. (2016). Modeling mechanical behavior of very coarse granular materials. *J. Engng Mech.* **143**, No. 1, C4016006.

Zhang, Y. D. & Buscarnera, G. (2014). Grainsize dependence of clastic yielding in unsaturated granular soils. *Granular Matter* **16**, No. 4, 469–483.

Zhang, Y. & Buscarnera, G. (2017). A rate-dependent breakage model based on the kinetics of crack growth at the grain scale. *Géotechnique* **67**, No. 11, 953–967, https://doi.org/10.1680/jgeot.16.P.181.

Zhang, Y. & Buscarnera, G. (2018). Breakage mechanics for granular materials in surface-reactive environments. *J. Mech. Phys. Solids* **112**, 89–108.

Zhang, Y. D., Buscarnera, G. & Einav, I. (2016). Grain size dependence of yielding in granular soils interpreted using fracture mechanics, breakage mechanics and Weibull statistics. *Géotechnique* **66**, No. 2, 149–160, https://doi.org/10.1680/jgeot.15.P.119.

Zhang, B., Chen, T., Peng, C., Qian, X. & Jie, Y. (2017). Experimental study on loading–creep coupling effect in rockfill material. *Int. J. Geomech.* **17**, No. 9, 04017059.

Zhou, W., Chang, X., Zhou, C. & Liu, X. (2010). Creep analysis of high concrete-faced rockfill dam. *Int. J. Numer. Methods Biomed. Engng* **26**, No. 11, 1477–1492.

Zhou, W., Hua, J., Chang, X., Yang, Q. & Ma, G. (2011a). Estimation of work status and deformation prediction of Shuibuya CFRD. *Chin. J. Geotech. Engng* **33**, No. S1, 65–70.

Zhou, W., Hua, J., Chang, X. & Zhou, C. (2011b). Settlement analysis of the Shuibuya concrete-face rockfill dam. *Comput. Geotech.* **38**, No. 2, 269–280.

Zhou, W., Li, S., Zhou, Z. & Chang, X. (2016). Remote sensing of deformation of a high concrete-faced rockfill dam using InSAR: a study of the Shuibuya dam, China. *Remote Sensing* **8**, No. 3, 255.

Zhu, S., Liang, X. P. & Feng, S. R. (2009). Back analysis of mechanical parameters of naturally graded rockfill materials based on large-scale loading plate tests. *Chin. J. Geotech. Engng* **31**, No. 6, 155–160.

Downloaded by [UNIV OF ILLINOIS] on [05/02/20]. Copyright © ICE Publishing, all rights reserved.